Physics and Chemistry of Minerals (2019) 46:607–621
https://doi.org/10.1007/s00269-019-01026-0

ORIGINAL PAPER

Phase transition and thermoelastic behavior of barite-group minerals at high-pressure and high-temperature conditions

Zhilin Ye[1,2] · **Bo Li**[1,2] · **Wei Chen**[3] · **Ruilian Tang**[4,5] · **Shijie Huang**[1,2] · **Jingui Xu**[1] · **Dawei Fan**[1] · **Wenge Zhou**[1] · **Maining Ma**[6] · **Hongsen Xie**[1]

Received: 28 November 2018 / Accepted: 1 February 2019 / Published online: 9 February 2019
© Springer-Verlag GmbH Germany, part of Springer Nature 2019

Abstract

Experimental studies on the phase transition and thermoelastic behavior of barite-group minerals are crucial to understand the recycle of sulfur in Earth's interior. Here, we present a high-pressure and high-temperature (high *P*–*T*) study on two barite-group minerals—barite ($BaSO_4$) and celestite ($SrSO_4$) up to ~59.5 GPa 700 K and ~22.2 GPa, 700 K, respectively, using in situ synchrotron-based X-ray diffraction (XRD) combined with diamond anvil cells (DACs). Our results show that $BaSO_4$ undergoes a pressure-induced phase transition from *Pbnm* to $P2_12_12_1$ at ~20.3 GPa, which is different from the previous results. Upon decompression, the high-pressure phase of $BaSO_4$ transforms back into its initial structure, which indicates a reversible phase transition. However, no phase transitions have been detected in $SrSO_4$ over the experimental *P*–*T* range. In addition, fitting a third-order Birch–Murnaghan equation of state to the pressure–volume data yields the bulk moduli and their pressure derivatives of $BaSO_4$ and $SrSO_4$. Simultaneously, the thermal expansion coefficients of $BaSO_4$ and $SrSO_4$ are also obtained, by fitting the temperature-volume data to the Fei-type thermal equation of state. Furthermore, the compositional effects on the phase transformation and thermoelastic behavior of barite-group minerals are also discussed, and the results suggest that the bond length of <M–O> (M=Ba, Sr, Pb) is an important factor that causes the phase transition pressure of $SrSO_4$ to be the largest, $PbSO_4$ is the second, and $BaSO_4$ is the lowest.

Keywords Sulfate · High temperature and high pressure · Synchrotron · X-ray diffraction · Equation of state · Diamond anvil cell

Introduction

As an abundant environment-influencing element, sulfur is not only vital in the evolution of life, but also a basic component of the ore-forming systems associated with subduction (Richards 2011; Tomkins and Evans 2015). Sulfur is transported into the deep Earth by the effective carrier of fluids or melts liberated from the subducted crust, while released into the atmosphere by magma degassing, dynamics of volcanic eruption, and redox evolution of magma (Evans 2012; Jégo and Dasgupta 2013, 2014; Wang et al. 2014; Tomkins and Evans 2015). Therefore, the recycling of sulfur in subduction zone is particularly important for biogeochemical cycles, the history of degassing of magmas, and the migration of ore metals (Canil and Fellows 2017). Sulfur exists in the forms of sulfide, sulfate minerals, sulfur-bearing fluids and melt in Earth's interior (Jégo and Dasgupta 2013). Some studies have suggested that the remarkable oxidized state of the mantle wedge originates from slab-derived sulfate

✉ Wenge Zhou
zhouwenge@vip.gyig.ac.cn

✉ Maining Ma
mamn@ucas.ac.cn

[1] Key Laboratory of High-Temperature and High-Pressure Study of the Earth's Interior, Institute of Geochemistry, Chinese Academy of Sciences, Guiyang 550081, China

[2] University of Chinese Academy of Science, Beijing 100049, China

[3] Guizhou Polytechnic of Construction, Guiyang 551400, China

[4] Center for High Pressure Science and Technology Advanced Research, Changchun 130012, China

[5] Changchun University of Science and Technology, Changchun 130022, China

[6] Key Laboratory of Computational Geodynamics, College of Earth and Planetary Sciences, University of Chinese Academy of Sciences, Beijing 100049, China

species (SO_4^{2-}) (Mungall 2002; Kelley and Cottrell 2009), indicating the importance of sulfate. Obviously, as common crust minerals and important sulfur-bearing minerals, the structural variation and thermoelastic properties of sulfates at high P–T conditions are necessary to improve our understanding on the existing forms of sulfur in Earth's interior (Kuang et al. 2017; Li et al. 2018).

Typical sulfate minerals in the deep Earth are anhydrite ($CaSO_4$), gypsum ($CaSO_4 \cdot 2H_2O$), barite ($BaSO_4$), celestite ($SrSO_4$), and anglesite ($PbSO_4$) (Gracia et al. 2012; Lee et al. 2013). Anhydrite and gypsum are not only the most important sulfate minerals, but also important component minerals in the crust. To date, the phase transformation characteristics of $CaSO_4$ have been extensively studied by experiment (e.g., XRD, Raman spectroscopy) and theoretical calculation (e.g., density functional theory) (e.g., Borg and Smith 1975; Crichton et al. 2005; Gracia et al. 2012; Fujii et al. 2016). Besides $CaSO_4$, barite-group minerals (celestite, barite, and anglesite) are also widely distributed in the crust (Lee et al. 2013). At ambient conditions, barite-group minerals are orthorhombic structure (*Pbnm*) and characterized by SO_4 tetrahedra and MO_{12} polyhedra (M=Sr, Pb, Ba). Each M atom coordinates with 12 oxygen atoms of six neighboring SO_4 groups to form a MO_{12} polyhedron, and SO_4 tetrahedra and MO_{12} polyhedra share edges (Fig. 1) (Garske and Peacor 1965; Miyake et al. 1978).

To date, a considerable number of experimental and theoretical investigations have been conducted to explore the structural phase transition of barite-group minerals. Previous synchrotron XRD studies show that $BaSO_4$ exists a pressure-induced phase transition at different pressures using different pressure media (Lee et al. 2003; Santamaría-Pérez et al. 2011). Simultaneously, Lee et al. (2003) also conducted the high-pressure Raman spectroscopic measurements on $BaSO_4$ and confirmed the pressure-induced phase transition by synchrotron XRD. Moreover, the theoretical calculation further indicated that the crystal structure of the high-pressure phase for $BaSO_4$ is also orthorhombic structure ($P2_12_12_1$) (Santamaría-Pérez et al. 2011). In contrast, Crichton et al. (2011) have not observed any pressure-induced phase transition of $BaSO_4$ to 21.5 GPa by Raman spectroscopic method. Therefore, experimental results of the pressure-induced phase transition of $BaSO_4$ are controversial. As an isostructural material with $BaSO_4$, the phase transition of $SrSO_4$ is controversial as well. Chen et al. (2010) observed a pressure-induced phase transition of $SrSO_4$ at ~ 12 GPa by Raman spectroscopic method. However, Kuang et al. (2017) have not observed any phase transition of $SrSO_4$ using in situ angle-dispersive XRD method to a maximum pressure of 15 GPa. Moreover, the previous studies of $SrSO_4$ are conducted under relatively poor hydrostatic conditions, which can significantly influence the structural phase transition. Hence, considering the controversy about the phase transition of $SrSO_4$, further experimental studies under better hydrostatic conditions are still essential to clarify its phase transition processes.

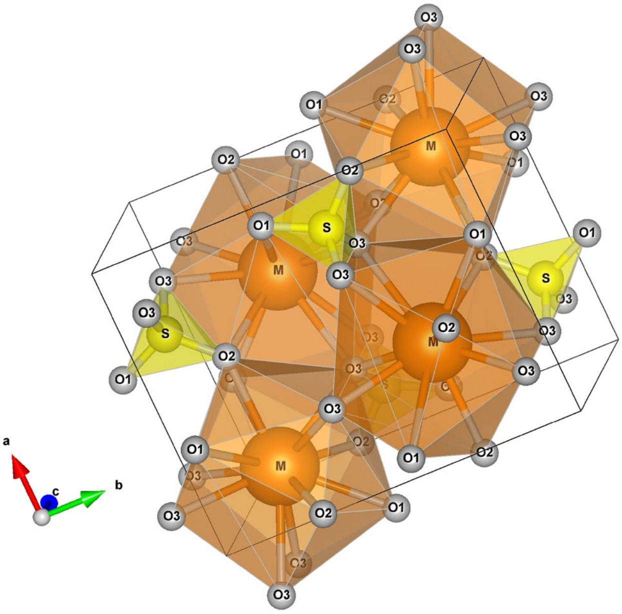

Fig. 1 Crystal structure of barite-group minerals at ambient pressure and room temperature (in *Pbnm*)

Insofar, the thermoelastic behavior of barite-group minerals has been the subject of several previous studies, but these experimental studies about the axial compression anisotropies of $BaSO_4$ and $SrSO_4$ are still controversial (Lee et al. 2003; Chen et al. 2010; Santamaría-Pérez et al. 2011; Kuang et al. 2017). In addition, the previous XRD studies on $BaSO_4$ were carried out at high temperatures, but have not provided the thermal expansion coefficient directly (Sawada and Takéuchi 1990). Furthermore, to the authors' knowledge, there are still no any existing relevant studies about the thermal properties of $SrSO_4$ at high temperatures. From the above, studying the compressibility and expansion of $BaSO_4$ and $SrSO_4$ at high P–T conditions are still needed to understand the thermoelastic behavior of barite-group minerals.

In this study, we have investigated the phase transition, compressibility, and thermal expansion of $BaSO_4$ and $SrSO_4$ at high-pressure/temperature conditions up to ~ 59.5 GPa and 700 K, ~ 22.2 GPa and 700 K, respectively, using the DACs combined with in situ angle-dispersive synchrotron XRD method. We find that $BaSO_4$ undergoes a pressure-induced phase transition, but no phase transition occurs in $SrSO_4$ over the current P–T range. We also obtain the compressibility and expansivities of $BaSO_4$ and $SrSO_4$. Moreover, combined with the previous results of $PbSO_4$, we also discuss the phase transitions, compressibility, and thermal expansion of barite-group minerals MSO_4 (M=Ba, Pb, and Sr).

Samples and experiments

Samples

The high-purity $BaSO_4$ and $SrSO_4$ samples (99.999%) in this study were purchased from Alfa Aesar Corporation. Both of them were ground in the agate mortar to an average size of 5 µm, and then were heated at 100 °C in the constant temperature furnace for 2 h to eliminate the absorbed water. The XRD pattern of samples under ambient conditions was obtained from the conventional power X-ray diffraction method with a D/Max-2200 X-ray diffractometer using graphite crystal monochromator and Cu Kα radiation. The ambient XRD spectrum of $BaSO_4$ and $SrSO_4$ was indexed according to the standard spectra of JCPDS83-1718 and JCPDS83-1719, respectively, confirming that the crystal structure of $BaSO_4$ and $SrSO_4$ is orthorhombic, and with *Pbnm* space group. In this study, to solve the controversy about the pressure-induced transition of $BaSO_4$ and $SrSO_4$ and obtain the thermal expansion coefficient accurately, the in situ synchrotron XRD experiments consist of two parts: ambient-temperature and high-pressure, and ambient-pressure and high-temperature experiments.

High-pressure experiments

Ambient-temperature and high-pressure experiments of $BaSO_4$ and $SrSO_4$ were carried out using symmetric piston cylinder DACs with pairs of 300 µm and 500 µm culet-size diamond anvils, respectively. The rhenium gaskets pre-indented to a thickness of ~45 µm and ~50 µm with a hole of 180 µm and 300 µm in diameter were used as the sample chamber for $BaSO_4$ and $SrSO_4$, respectively. In both experiments, a piece of sample disk was loaded into the sample chamber with a gold tablet as the pressure calibrant (Fei et al. 2007). The XRD patterns of gold were collected before and after sample data collection for each pressure, and the average pressure values were used for equation of state (EoS) calculation. Neon gas was used as the pressure-transmitting medium (Hemley et al. 1989), by the gas-loading system at Center for High-Pressure Science and Technology Advanced Research (HPSTAR), China.

In situ ambient-temperature and high-pressure synchrotron XRD experiments were carried out at the BL15U1 beamline of Shanghai Synchrotron Radiation Facility (SSRF). The incident wavelength of the monochromatic beam was 0.6199 Å and the X-ray beam was focused to a beam size of 2×3 µm^2. The sample-to-detector distance and the geometrical parameters of the detector were calibrated with cerium dioxide (CeO_2). Diffraction data of the samples were collected by a MAR-165 charge-couple device (CCD) detector, and then were integrated as a function of 2θ using the Fit2D program (Hammersley et al. 1996). Further analyses and refinements of high-pressure XRD patterns were performed by means of the profile-fitting technique implemented in the EXPGUI/GSAS software package (Larson and Von Dreele 2004). Refinement of peak positions and extraction of unit-cell parameters were analyzed by the Le Bail method (Le Bail et al. 1988). The initial unit-cell parameters, unit-cell coordinates, and space group were stemmed from Miyake et al. (1978). The sequence of the full-matrix least-squares fitting was refined by changing the unit-cell parameters, background, and profile function parameters. Until the end of the refinement, all the unit-cell parameters should be changed simultaneously, and the refinement approached convergence.

High-temperature experiments

Ambient-pressure and high-temperature experiments were carried out using an externally heating DAC (Fan et al. 2010, 2014) equipped with two pairs of 400 µm and 500 µm culets-size diamond anvils for $BaSO_4$ and $SrSO_4$, respectively. The pre-indented T301 stainless steel foil gaskets with thickness of 60–80 µm were drilled with diameter of 280–300 µm holes as the sample chambers. Heating was carried out using NiCr resistor wire with a diameter of 0.3 mm as an external heating device. The experimental temperature was measured by a $Pt_{90}Rh_{10}$–Pt_{100} thermocouple attached to the pavilion of the diamond anvil, and its precision was ± 2 °C. The $BaSO_4$ and $SrSO_4$ powders were slightly formed approximately 50-µm-thick disks, and a piece of sample about 200 µm in diameter was loaded into the sample chamber without any pressure-transmitting medium. The ambient-pressure and high-temperature experimental process is as follows. The temperature was first increased from ambient-temperature to the maximum temperature of 700 K, and then, temperature was kept for ~600 s to relax the sample before collection of the XRD spectrum. Then, the temperature was dropped to 320 K in 30 K steps. For each temperature point, an XRD pattern was collected, and the typical exposure time for collecting these XRD patterns of samples was 300 s. Additional details of the experimental setup and DAC assembly were given in Fan et al. (2010).

The ambient-pressure and high-temperature synchrotron XRD experiments were conducted at the 4W2 beamline of Beijing Synchrotron Radiation Facility (BSRF). Diffraction patterns were collected using an image plate detector (MAR-345). The incident X-ray beam was monochromatized to a wavelength of 0.6199 Å and the beam size was collimated to 20×30 µm^2. CeO_2 was used as the diffraction standard. The process of integrate diffraction patterns and further analysis of high-temperature XRD data were the same as ambient-temperature and high-pressure XRD experiments.

Results

Figure 2 shows the typical pressure evolution of the XRD patterns of $BaSO_4$, where all of the peaks shift to higher 2θ angle and the intensity of some peaks become slightly weak and broad with increasing pressure. However, a new peak appears at $2\theta = 10.086°$ when pressure increases to ~20.3 GPa. Further increase pressure to ~26.6 GPa, another new peak appears at $2\theta = 12.037°$. These significant changes indicate that $BaSO_4$ undergoes a pressure-induced phase transition. In addition, with continuous increasing pressure, the intensity of these new peaks increases and obviously split. These new diffraction peaks from the new high-pressure phase are stable up to the maximum pressure (59.5 GPa) in this study, which indicates that there is no further phase transition of $BaSO_4$. Upon decompression, the high-pressure phase of $BaSO_4$ transforms back to its original structure (on the top of Fig. 2), which demonstrates that $BaSO_4$ undergoes a reversible phase transition at ~20.3 GPa. Previous experimental and theoretical results show that the crystal structure of the new high-pressure phase of $BaSO_4$ is $P2_12_12_1$ structure (Santamaría-Pérez et al. 2011). Hence, it is reasonable to infer that $P2_12_12_1$ structure is the most possible high-pressure phase of $BaSO_4$. We thus fit the XRD patterns of the high-pressure phase using the $P2_12_12_1$ structure, but the fitting results are unsatisfactory. Nevertheless, we obtain excellent fitting results using the $P2_12_12_1 + Pbnm$ structure to fit the XRD patterns of the high-pressure phase. The Le Bail refinements show an excellent agreement between calculated and experimental results using GSAS program (Fig. 3), and give satisfying fitting results with $R_{wp} = 0.9\%$ and $R_p = 0.54\%$. Therefore, we infer that $BaSO_4$ undergoes a pressure-induced phase transition from $Pbnm$ to $P2_12_12_1$, but this phase does not completely immediately and there is a two-phase coexistence zone at pressures above 20 GPa. Moreover, up to the maximum pressure (59.5 GPa) in this study, we still obtain better fitting results using $P2_12_12_1 + Pbnm$ structures than only using $P2_12_12_1$ structure, which means that the two phases of $Pbnm$ and $P2_12_12_1$ may still coexist at pressures up to ~60 GPa.

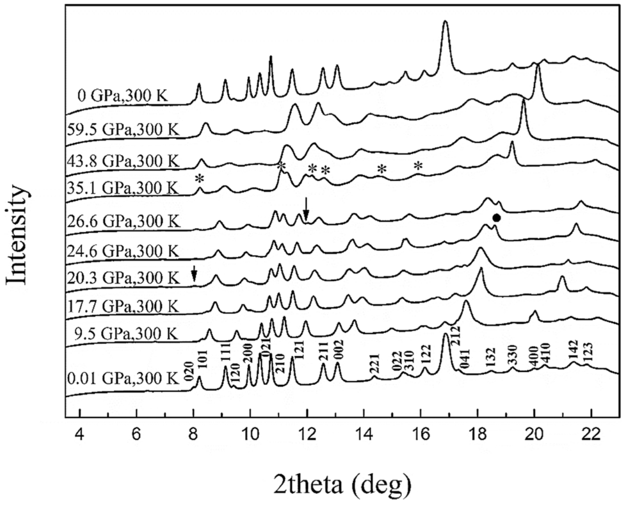

Fig. 2 Representative X-ray diffraction patterns of $BaSO_4$ obtained in this study up to 59.5 GPa at room temperature. The appearance of new peaks for $BaSO_4$ has been observed in the experimental process at 20.3 GPa and 26.6 GPa, respectively. Asterisks indicate the peak indices of $P2_12_12_1$ phase, which are (011), (021), (121), (201), (031), and (112). Black solid dot indicates diffraction peaks from the pressure-transmitting medium Neon

Moreover, typical XRD patterns of $SrSO_4$ at high pressure are also shown in Fig. 4. With increasing pressure, all peaks just shift toward higher 2θ angles and become slightly broad and weak. It is noteworthy that a new peak appears at 12.4 GPa in the region of 17°–19°, which is confirmed to be a peak of Neon pressure medium at this pressure condition. However, besides this Neon peak, neither the disappearance of peaks nor appearance of other new peaks has been observed in the pressure range of this study. Therefore, $SrSO_4$ does not undergo phase transition under the pressure range in this study. The typical refinement results of $SrSO_4$ at high pressure are shown in Fig. 5.

The typical temperature evolution of the XRD patterns for $BaSO_4$ and $SrSO_4$ is shown in Fig. 6, where all the peaks for $BaSO_4$ and $SrSO_4$ shift toward lower 2θ angle with increasing temperature from 315 to 320 K to 700 K at ambient pressure. Neither the disappearance of peaks nor appearance of new peaks has been observed in the temperature range of these experiments, indicating that $BaSO_4$ and $SrSO_4$ remain stable without any temperature-induced phase transition. The typical refinement results of $BaSO_4$ and $SrSO_4$ at high temperature are shown in Fig. 7.

The unit-cell parameters of $BaSO_4$ and $SrSO_4$ at high-pressure conditions are shown in Tables 1 and 2, respectively. The P–V data are fitted with the third-order Birch–Murnaghan EoS to obtain the elastic parameters (Birch 1947):

$$P = \left(\frac{2}{3}\right)\mathrm{K}_0\left[\left(V_0/V\right)^{7/3} - \left(V_0/V\right)^{5/3}\right] \times \left\{1 + (3/4)\left(K_0' - 4\right)\left[\left(V_0/V\right)^{2/3} - 1\right]\right\},$$

where V_0, V, K_0, and K_0' are the zero-pressure unit-cell volume, and high-pressure unit-cell volume, isothermal bulk modulus, and its pressure derivative at ambient conditions, respectively. The results obtained from least-squares fitting by Eos-Fit program (Gonzalez-Platas et al. 2016) are

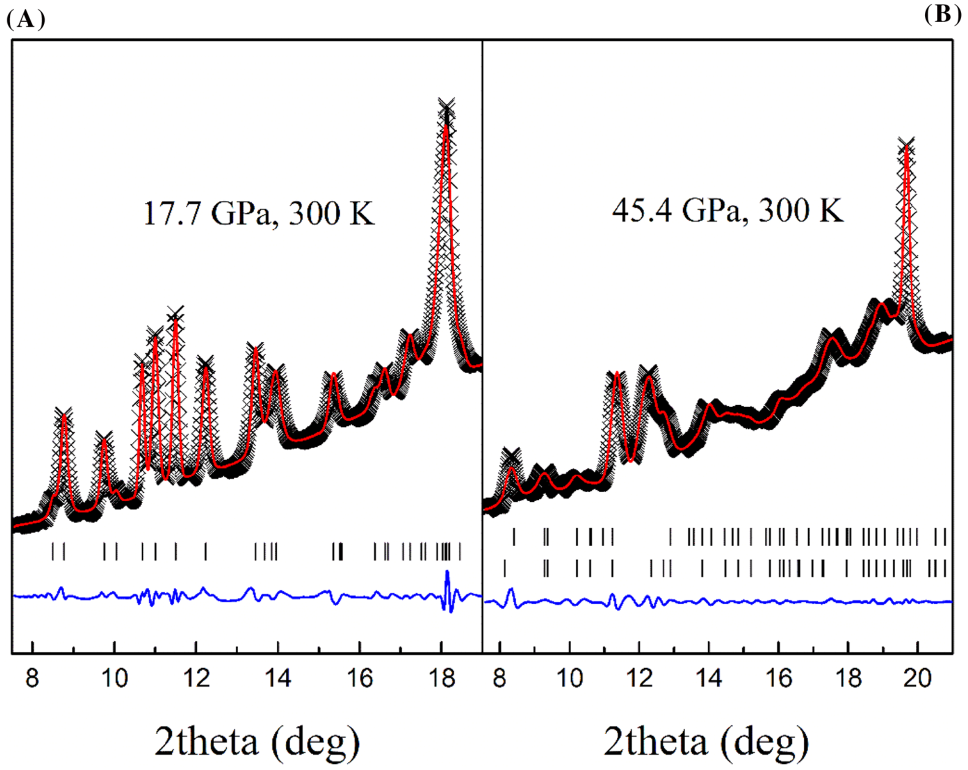

Fig. 3 La Bail profile fit of the diffraction profile of $BaSO_4$ at 17.7 GPa (**a**) and Rietveld profile fit of the diffraction profile at 45.4 GPa at room temperature (**b**). Observed spectra (black line), fitted spectra (red solid line), difference plot (blue solid line), and Bragg peak positions (tick marks) are shown

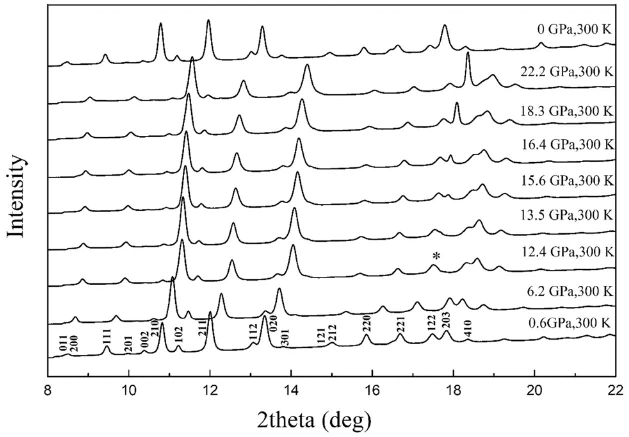

Fig. 4 Representative X-ray diffraction patterns of $SrSO_4$ obtained in this study up to 22.2 GPa at room temperature. Asterisk indicates diffraction peaks from the pressure-transmitting medium Neon

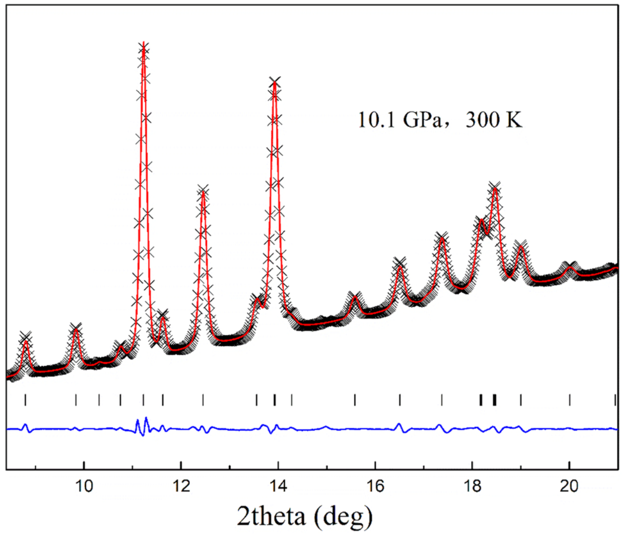

Fig. 5 La Bail profile fit of the diffraction profile of $SrSO_4$ at 10.1 GPa at room temperature. Observed spectra (black line), fitted spectra (red solid line), difference plot (blue solid line), and Bragg peak positions (tick marks) are shown

$V_0 = 344.173$ (1) Å^3, $K_0 = 58$ (2) GPa, $K_0' = 4.2$ (4) of $BaSO_4$ and $V_0 = 306.846$ (1) Å^3, $K_0 = 64$ (2) GPa, $K_0' = 4.8$ (4) of $SrSO_4$. When fix $K_0' = 4$, the fitting results yield $K_0 = 60$ (1) GPa and $K_0 = 68$ (1) GPa of $BaSO_4$ and $SrSO_4$, respectively. The unit-cell volume variation of $BaSO_4$ and $SrSO_4$ as a function of pressure and the compression curve calculated by these fitted parameters are plotted in Fig. 8, where only the data before the phase transition of $BaSO_4$ are selected for fitting. To evaluate the quality of the third-order Birch–Murnaghan EoS fitting, the relationship between the Eulerian strain $\left(f_E = \left[\left(V_0/V\right)^{2/3} - 1\right]\right)$ and normalized pressure $\left(F_E = P/\left[3fE\left(2f_E + 1\right)^{5/2}\right]\right)$ (Angel 2000) of $BaSO_4$ and $SrSO_4$ are plotted and shown in Fig. 9. Both sets of data show a slightly positive slope (Fig. 9) which

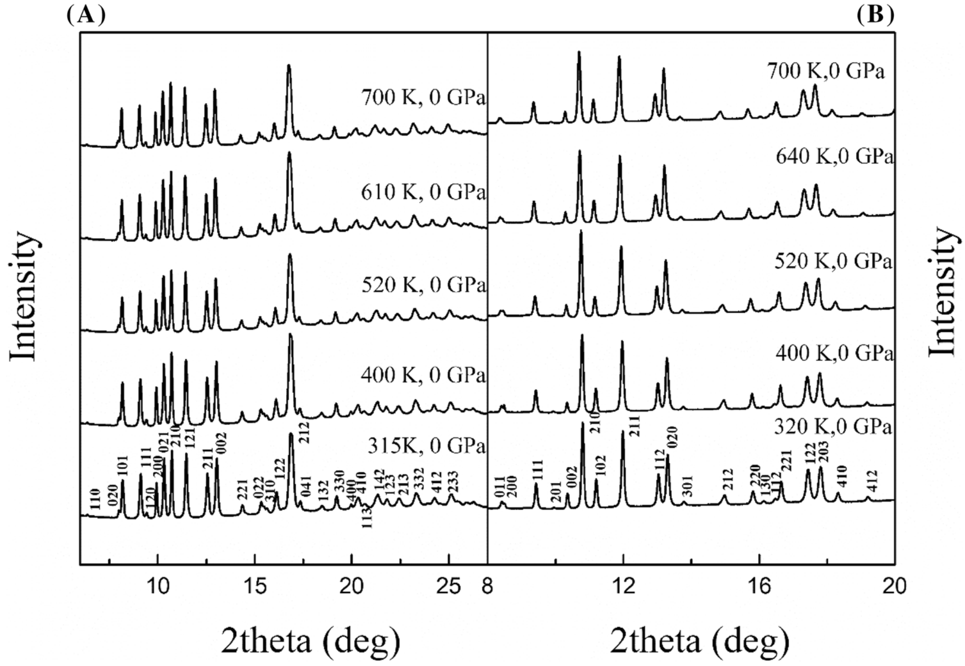

Fig. 6 Representative X-ray diffraction patterns of $BaSO_4$ (**a**) and $SrSO_4$ (**b**) obtained in this study up to 700 K at ambient pressure

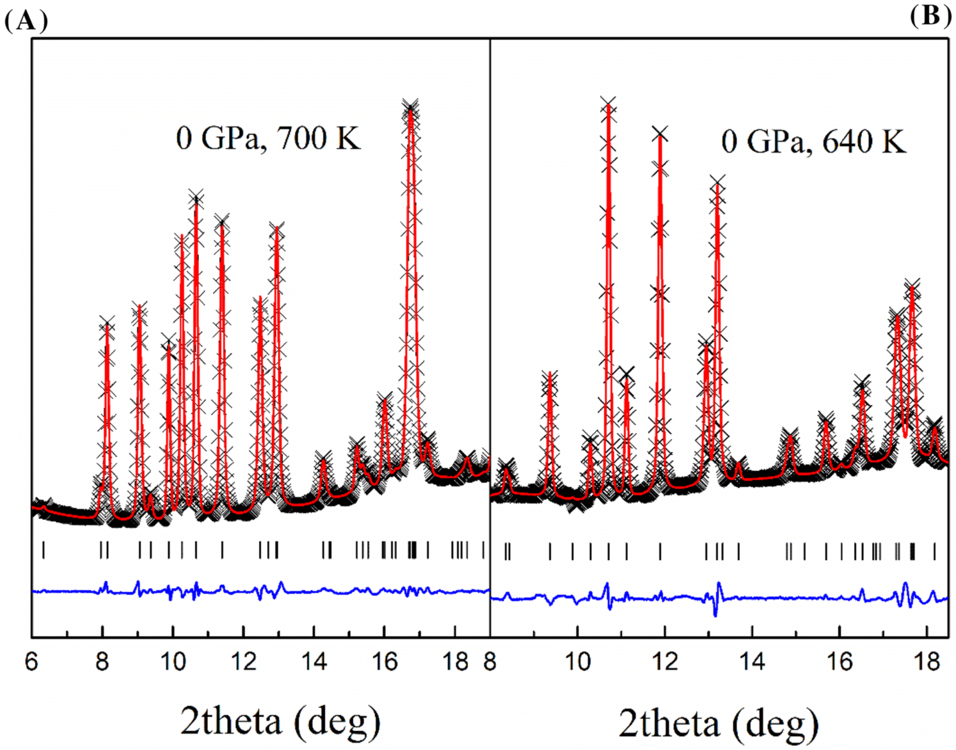

Fig. 7 La Bail profile fit of the diffraction profile of $BaSO_4$ at 700 K at ambient pressure (**a**) and $SrSO_4$ at 640 K at ambient pressure (**b**). Observed spectra (black line), fitted spectra (red solid line), difference plot (blue solid line), and Bragg peak positions (tick marks) are shown

indicates that the pressure derivative of the bulk modulus (K_0') is higher than 4. In addition, the weighted linear regression through the data points yields the intercept value, F_E (0) = 58 (1) GPa for $BaSO_4$ and F_E (0) = 64 (1) GPa for $SrSO_4$, which is absolutely consistent with the isothermal bulk modulus K_0 = 58 (2) GPa and K_0 = 64 (2) GPa obtained by the third-order Birch–Murnaghan EoS fitting, respectively. Therefore, the third-order Birch–Murnaghan EoS is reasonable to describe the *P*–*V* data for $BaSO_4$ and $SrSO_4$ in this study.

Table 1 Unit-cell parameters in $BaSO_4$ at ambient temperature and high pressure

P (GPa)	a (Å)	b (Å)	c (Å)	V (Å)
0.0001	7.1371 (2)	8.8656 (4)	5.4384 (3)	344.11 (3)
0.7	7.1117 (2)	8.8384 (6)	5.4170 (3)	340.49 (3)
1.8	7.0695 (2)	8.7929 (4)	5.3800 (3)	334.43 (3)
2.7	7.0341 (2)	8.7513 (5)	5.3511 (3)	329.40 (3)
3.9	6.9907 (3)	8.7075 (6)	5.3180 (4)	323.68 (4)
4.6	6.9816 (2)	8.6974 (6)	5.3077 (3)	322.29 (3)
4.9	6.9651 (2)	8.6790 (4)	5.2967 (2)	320.19 (2)
5.9	6.9307 (2)	8.6409 (5)	5.2726 (3)	315.76 (3)
7.3	6.8898 (3)	8.6019 (8)	5.2410 (4)	310.60 (4)
7.5	6.8868 (2)	8.5985 (6)	5.2409 (3)	310.34 (3)
7.8	6.8787 (2)	8.5917 (6)	5.2310 (4)	309.16 (3)
8.7	6.8533 (2)	8.5663 (5)	5.2157 (3)	306.20 (3)
9.5	6.8359 (3)	8.5407 (7)	5.2069 (3)	304.00 (3)
10.5	6.8024 (3)	8.5109 (7)	5.1817 (4)	300.00 (4)
11.6	6.7771 (3)	8.4839 (7)	5.1690 (5)	298.20 (4)
13.2	6.7519 (3)	8.4628 (7)	5.1483 (4)	294.18 (4)
13.8	6.7410 (2)	8.4324 (6)	5.1288 (4)	291.54 (3)
14.5	6.7202 (3)	8.4192 (9)	5.1194 (6)	289.65 (5)
15.9	6.7045 (3)	8.3669 (9)	5.0934 (7)	285.72 (5)
17.7	6.6897 (3)	8.3518 (8)	5.0715 (5)	283.35 (4)

Numbers in parenthesis represent standard deviations

Table 2 Unit-cell parameters in $SrSO_4$ at ambient temperature and high pressure

P (GPa)	a (Å)	b (Å)	c (Å)	V (Å)
0.6	6.8479 (2)	8.3379 (2)	5.3322 (1)	304.45 (1)
0.6	6.8440 (3)	8.3323 (2)	5.3282 (1)	303.84 (2)
1.0	6.8315 (3)	8.3204 (2)	5.3156 (1)	302.14 (2)
1.7	6.8083 (2)	8.2904 (2)	5.2936 (1)	298.80 (1)
2.5	6.7858 (2)	8.2641 (2)	5.2733 (1)	295.72 (1)
3.6	6.7608 (2)	8.2341 (2)	5.2500 (1)	292.27 (1)
4.8	6.7330 (3)	8.1953 (3)	5.2198 (2)	288.02 (2)
5.6	6.7145 (4)	8.1804 (3)	5.2022 (2)	285.75 (2)
6.2	6.7011 (3)	8.1680 (2)	5.1901 (1)	284.08 (2)
6.8	6.6835 (3)	8.1493 (2)	5.1742 (1)	281.82 (2)
7.2	6.6738 (4)	8.1382 (3)	5.1671 (2)	280.64 (2)
7.9	6.6576 (5)	8.1204 (3)	5.1523 (2)	278.54 (3)
8.7	6.6449 (4)	8.1055 (4)	5.1359 (4)	276.62 (3)
9.4	6.6239 (3)	8.0867 (5)	5.1215 (4)	274.34 (3)
10.1	6.6082 (4)	8.0712 (3)	5.1059 (2)	272.33 (2)
10.9	6.5900 (5)	8.0483 (3)	5.0903 (2)	269.98 (2)
11.5	6.5758 (5)	8.0346 (3)	5.0789 (2)	268.34 (2)
12.4	6.5593 (6)	8.0187 (3)	5.0616 (2)	266.22 (3)
13.5	6.5449 (5)	8.0019 (3)	5.0477 (2)	264.36 (3)
14.2	6.5335 (5)	7.9919 (3)	5.0384 (2)	263.08 (3)
14.9	6.5202 (7)	7.9788 (4)	5.0278 (2)	261.56 (3)
15.6	6.5122 (6)	7.9646 (3)	5.0202 (1)	260.38 (3)
16.4	6.4962 (8)	7.9453 (3)	5.0080 (2)	258.48 (4)
17.0	6.4901 (6)	7.9388 (2)	5.0043 (1)	257.84 (3)
17.6	6.4809 (6)	7.9305 (3)	4.9942 (2)	256.68 (3)
18.3	6.4682 (6)	7.9164 (2)	4.9834 (1)	255.17 (2)
19.3	6.4519 (6)	7.9006 (2)	4.9705 (1)	253.37 (3)
19.9	6.4455 (6)	7.8885 (2)	4.9630 (1)	252.35 (6)
20.6	6.4356 (9)	7.8801 (3)	4.9554 (2)	251.30 (4)
21.1	6.4269 (6)	7.8711 (3)	4.9471 (1)	250.26 (3)
22.2	6.4148 (7)	7.8599 (3)	4.9372 (1)	248.93 (3)

Numbers in parenthesis represent standard deviations

The axial compressibility of $BaSO_4$ and $SrSO_4$ as functions of pressure are plotted in Fig. 10. Fitting the unit-cell parameters at room temperature by a "linearized" third-order Birch–Murnaghan EoS with Eos-Fit program (Gonzalez-Platas et al. 2016) obtain the unit-cell parameters and the axial elastic parameters of $BaSO_4$ and $SrSO_4$. The unit-cell parameters of $BaSO_4$ and $SrSO_4$ are $a_0 = 7.138$ (1) Å, $b_0 = 8.866$ (1) Å, $c_0 = 5.439$ (1) Å and $a_0 = 6.864$ (1) Å, $b_0 = 8.358$ (1) Å, $c_0 = 5.348$ (1) Å and the refined axial moduli of $BaSO_4$ and $SrSO_4$ are $K_{a0} = 169$ (2) GPa, $K_{b0} = 203$ (2) GPa, $K_{c0} = 164$ (2) GPa and $K_{a0} = 214$ (2) GPa, $K_{b0} = 237(3)$ GPa, $K_{c0} = 167$ (2) GPa, respectively, at ambient pressure. According to the following form of ambient-pressure axial compressibility $\beta\iota$ (Xia et al. 1998; Fan et al. 2010, 2015):

$$\beta_1 = \frac{1}{(3M_1)}.$$

The ambient-pressure axial compressibility of a-, b-, and c-axes are 1.97 (2) × 10^{-3}, 1.64 (2) × 10^{-3}, 2.03 (2) × 10^{-3} GPa^{-1} for $BaSO_4$ and 1.56 (2) × 10^{-3}, 1.41 (3) × 10^{-3}, and 2.00 (2) × 10^{-3} GPa^{-1} for $SrSO_4$. This clearly shows that both $BaSO_4$ and $SrSO_4$ have axial compressive anisotropy. For $BaSO_4$, b-axial is the most incompressible and the compressibility along a-axis and c-axis is almost equivalent (Fig. 10). Meanwhile, the compressibility of $SrSO_4$ along c-axis is the most, followed by a-axis and b-axis (Fig. 10). There is a good consistency of b-axis compressibility between $BaSO_4$ and $SrSO_4$.

Thermal expansion coefficients of $BaSO_4$ and $SrSO_4$ are obtained from the T–V data (Tables 3, 4) up to 700 K at ambient pressure. The thermal expansion expression proposed by Fei (1995) is fitted to calculate our ambient-pressure and high-temperature data with the following form:

$$V_{0T} = V_0 \exp\left(\alpha_0\left(T - T_{ref}\right) + \frac{1}{2}\alpha_1\left(T^2 - T_{ref}{}^2\right) - \alpha_2\left(\frac{1}{T} - \frac{1}{T_{ref}}\right)\right),$$

where V_0 represents the unit-cell volume at room temperature, and α_0, α_1, and α_2 are the parameters for the thermal

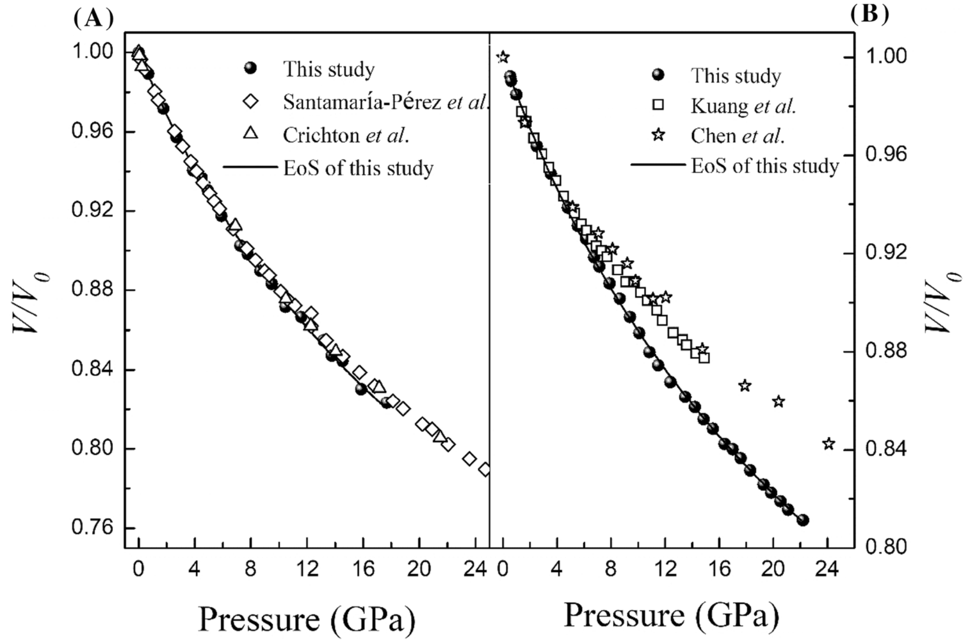

Fig. 8 Comparison of *P*–*V* data of $BaSO_4$ (**a**) and $SrSO_4$ (**b**) at room temperature with predecessors

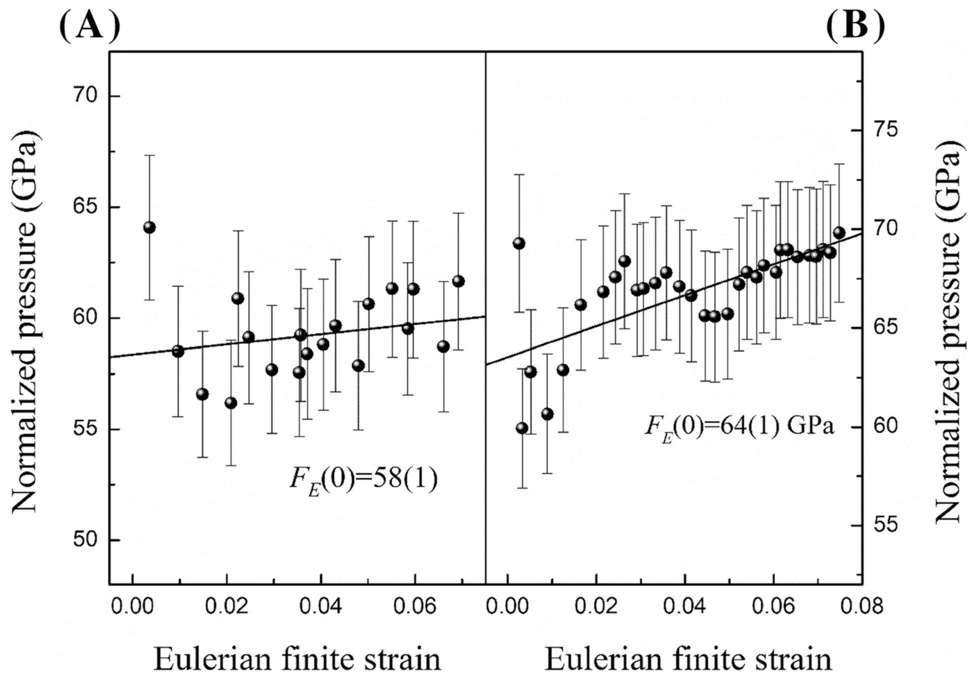

Fig. 9 Eulerian finite stain-normalized pressure (F_E–f_E) plot of $BaSO_4$ (**a**) and $SrSO_4$ (**b**). The solid lines represent the linear fit through the data

expansion α as a function of temperature $a = a_0+a_1T+a_2T^{-2}$. Considering the limited data at high temperatures, we use the simplified form $a = a_0+a_1T$. Using the above equations to fit our high-temperature data with the Eos-Fit program (Gonzalez-Platas et al. 2016), the volumetric thermal expansion coefficients for $BaSO_4$ and $SrSO_4$ are $a_V=2.52\ (24)\times10^{-5}+5.25\ (54)\times10^{-8}\times T$, and $a_V=2.52\ (24)\times10^{-5}+8.48\ (51)\times10^{-8}\times T$ within 300–700 K, where the volumetric thermal expansion coefficients at ambient conditions are $4.091\times10^{-5}\ K^{-1}$ for $BaSO_4$ and $5.061\times10^{-5}\ K^{-1}$ for $SrSO_4$, respectively (Fig. 11). Simultaneously, the axial thermal expansion coefficients of $BaSO_4$ along *a*-, *b*-, and *c*-axes are $a_a=0.66\ (6)\times10^{-5}+1.75\ (12)\times10^{-8}\times T$, $a_b=0.92\ (10)\times10^{-5}+1.50\ (23)\times10^{-8}\times T$, and $a_c=1.25\ (11)\times10^{-5}+1.43\ (24)\times10^{-8}\times T$, respectively. At ambient conditions, $a_{a0}=1.18\times10^{-5}\ K^{-1}$, $a_{b0}=1.36\times10^{-5}\ K^{-1}$, and $a_{c0}=1.\ 67\times10^{-5}\ K^{-1}$ for $BaSO_4$ along *a*-, *b*-, and *c*-axes (Fig. 12a). The obtained

Fig. 10 Pressure dependence of the unit-cell parameters *a, b*, and *c* of $BaSO_4$ (**a**) and $SrSO_4$ (**b**) at room temperature

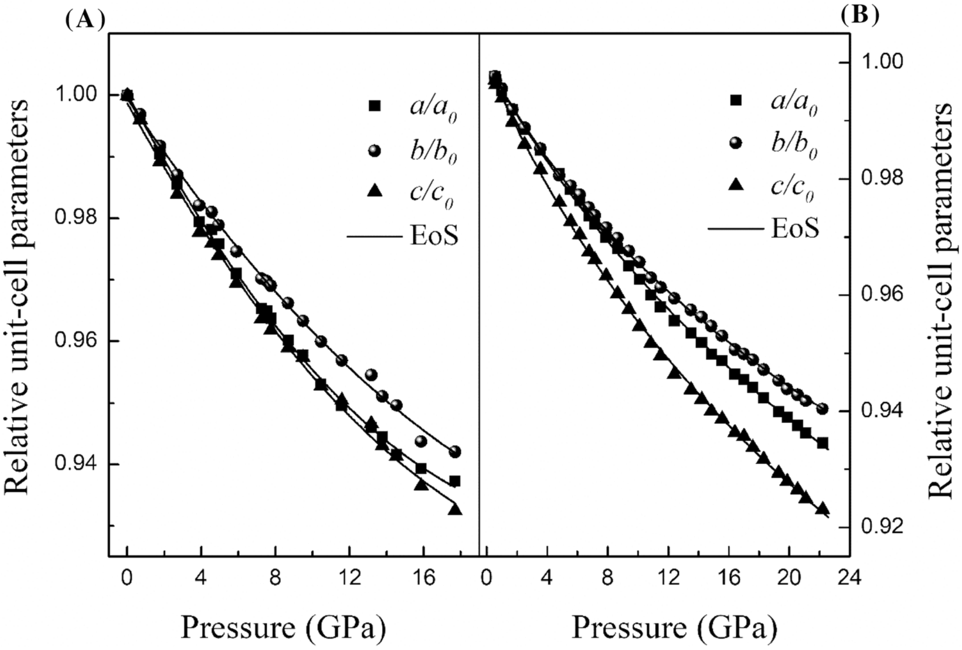

Table 3 Unit-cell parameters in $BaSO_4$ at high temperature and room pressure

T (K)	*a* (Å)	*b* (Å)	*c* (Å)	*V* (Å^3)
315	7.1449 (1)	8.8683 (3)	5.4501 (1)	345.33 (2)
340	7.1472 (1)	8.8712 (3)	5.4528 (1)	345.73 (1)
370	7.1499 (1)	8.8753 (3)	5.4556 (1)	346.20 (2)
400	7.1526 (1)	8.8785 (3)	5.4585 (1)	346.64 (2)
430	7.1550 (1)	8.8811 (3)	5.4601 (2)	346.95 (2)
460	7.1584 (2)	8.8876 (4)	5.4641 (2)	347.63 (2)
490	7.1624 (2)	8.8907 (4)	5.4665 (2)	348.10 (2)
520	7.1655 (2)	8.8966 (2)	5.4712 (1)	348.78 (2)
550	7.1690 (1)	8.9012 (3)	5.4743 (1)	349.33 (2)
580	7.1720 (1)	8.9056 (4)	5.4771 (2)	349.83 (2)
610	7.1758 (1)	8.9101 (3)	5.4812 (1)	350.45 (2)
640	7.1798 (2)	8.9148 (3)	5.4880 (2)	350.99 (2)
670	7.1838 (1)	8.9207 (4)	5.4883 (2)	351.71 (2)
700	7.1873 (1)	8.9250 (3)	5.4914 (2)	352.25 (2)

Numbers in parenthesis represent standard deviations

Table 4 Unit-cell parameters in $SrSO_4$ at high temperature and room pressure

T (K)	*a* (Å)	*b* (Å)	*c* (Å)	*V* (Å^3)
320	6.8603 (4)	8.3494 (4)	5.3465 (2)	306.24 (3)
340	6.8625 (4)	8.3527 (4)	5.3481 (2)	306.56 (3)
370	6.8657 (4)	8.3574 (4)	5.3507 (2)	307.02 (3)
400	6.8686 (5)	8.3612 (5)	5.3542 (3)	307.49 (3)
430	6.8718 (5)	8.3672 (2)	5.3573 (2)	308.03 (3)
460	6.8765 (5)	8.3729 (5)	5.3614 (3)	308.69 (3)
490	6.8809 (6)	8.3801 (6)	5.3654 (3)	309.38 (4)
520	6.8838 (6)	8.3863 (6)	5.3688 (3)	309.94 (4)
550	6.8874 (6)	8.3924 (6)	5.3733 (3)	310.58 (4)
580	6.8919 (6)	8.3984 (6)	5.3780 (4)	311.28 (4)
610	6.8974 (6)	8.4062 (6)	5.3821 (3)	312.06 (4)
640	6.9023 (6)	8.4149 (6)	5.3862 (3)	312.84 (4)
670	6.9045 (3)	8.4261 (3)	5.3880 (1)	313.51 (2)
700	6.9090 (2)	8.4329 (2)	5.3929 (1)	314.20 (2)

Numbers in parenthesis represent standard deviations

axial thermal expansion coefficients of $SrSO_4$ along *a*-, *b*-, and *c*-axes are $a_a = 1.14\ (11) \times 10^{-5} + 1.45\ (23) \times 10^{-8} \times T$, $a_b = -0.06\ (11) \times 10^{-5} + 5.25\ (24) \times 10^{-8} \times T$, and $a_c = 1.49\ (15) \times 10^{-5} + 1.63\ (31) \times 10^{-8} \times T$, respectively. These values at ambient conditions are $a_{a0} = 1.57 \times 10^{-5}\ K^{-1}$, $a_{b0} = 1.52 \times 10^{-5}\ K^{-1}$, and $a_{c0} = 1.98 \times 10^{-5}\ K^{-1}$ for $SrSO_4$ along *a*-, *b*-, and *c*-axes (Fig. 12b). The ratios of axial thermal expansion coefficients at 300K of $BaSO_4$ and $SrSO_4$ are 1.00:1.15:1.42 and 1.03:1.00:1.30, respectively. The axial thermal expansion of $BaSO_4$ and $SrSO_4$ is slightly anisotropic, where the *c*-axis of $BaSO_4$ exhibits a much larger thermal expansion coefficient than those along *a*-, and *b*-axes, but *b*-axis of $SrSO_4$ has larger thermal expansion coefficient than those along *a*- and *c*-axes. It is worth noting that *c*-axis of $BaSO_4$ has the most compressibility as well as thermal expansivity.

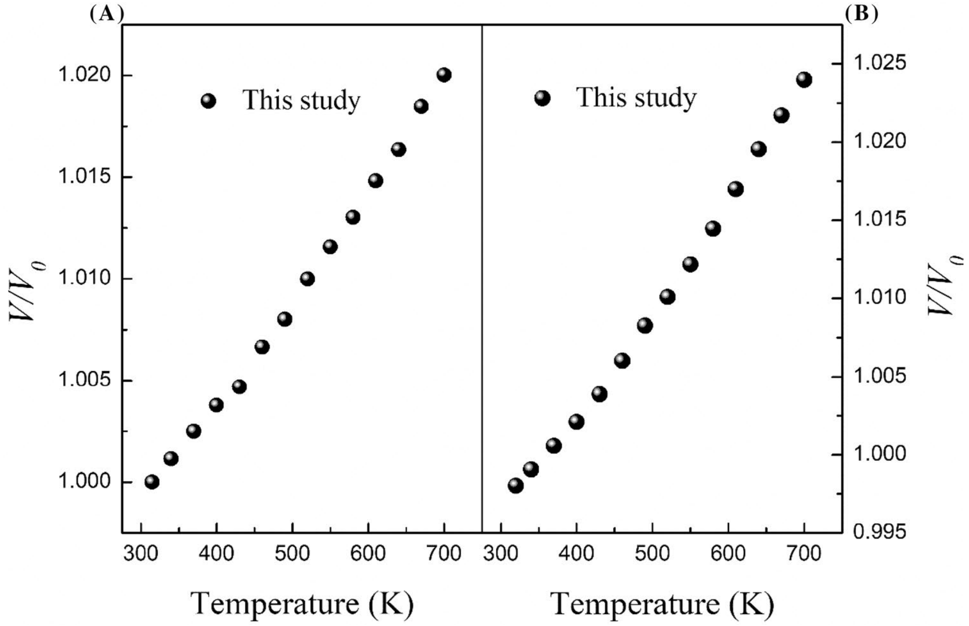

Fig. 11 *T*–*V* data of $BaSO_4$ (**a**) and $SrSO_4$ (**b**) at ambient pressure

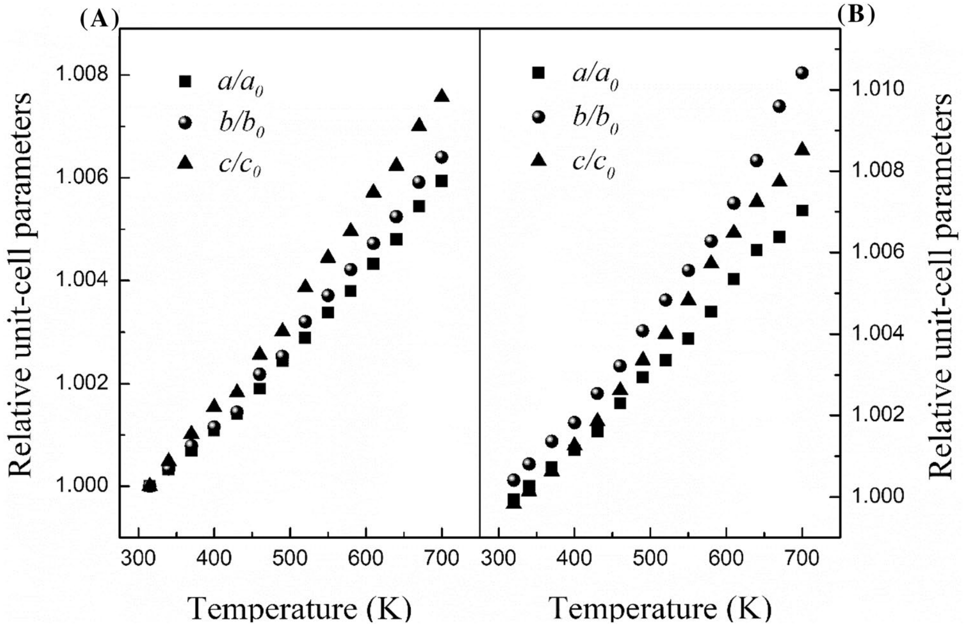

Fig. 12 Temperature dependence of the unit-cell parameters *a, b*, and *c* of $BaSO_4$ (**a**) and $SrSO_4$ (**b**) at ambient pressure

Discussion

Pressure-induced phase transition of barite-group minerals

$BaSO_4$

Our results confirm that $BaSO_4$ exists a pressure-induced reversible phase transition from *Pbnm* to $P2_12_12_1$ at ~ 20.3 GPa. A comparison of our results with the previous results shows that $BaSO_4$ undergoes a pressure-induced phase transition, but the phase transition pressure is still inconclusive. Santamaría-Pérez et al. (2011) obtained the phase transition pressures were ~ 17 GPa, ~ 19 GPa, and ~ 27 GPa using different pressure-transmitting mediums (methanol–ethanol mixture, silicone oil, and He, respectively) by synchrotron XRD. Similarly, Lee et al. (2003) also observed a reversible phase transition of $BaSO_4$ at ~ 10 GPa without any pressure-transmitting medium (Lee et al. 2003). On the contrary, Crichton et al. (2011) have not observed any phase transition of $BaSO_4$ by XRD and Raman spectroscopy methods up to 21.5 GPa using He as pressure-transmitting medium. From the above analysis, we can conclude that the hydrostatic environment provided by different pressure-transmitting media can result in the different phase transition pressures of $BaSO_4$. The better hydrostatic environment may drive the phase transition to occur at higher pressures.

$SrSO_4$

Until now, it is still controversial about whether $SrSO_4$ exists the pressure-induced phase transition. Chen et al. (2010) concluded relevant Raman spectroscopy and XRD measurements of $SrSO_4$ at high pressure. They observed a discontinuity in the slope ($d\nu_1/dp$) of vibration and a disappearance of the (201) diffraction peak at ~ 11–12 GPa, and they inferred that $SrSO_4$ exists a pressure-induced phase transition. However, the discontinuity in the slope ($d\nu_1/dp$) of Raman vibration showed in the study of Chen et al. (2010) was not clear. In addition, Chen et al. (2010) used 4:1 methanol–ethanol mixture as a pressure-transmitting medium that could result in relatively low quality of experimental data. Therefore, we estimate that there is not enough evidence to prove that $SrSO_4$ has undergone a pressure-induced phase transition. Recently, Kuang et al. (2017) conducted the in situ synchrotron XRD measurements of $SrSO_4$ up to 15 GPa at ambient temperature without observing any phase transition that is consistent with this study. However, the pressure-transmitting medium used in the previous studies were 4:1 methanol–ethanol mixture or 16:3:1 methanol–ethanol–water mixture, which could not maintain a good hydrostatic environment and cause nonhydrostatic stress in the sample chambers at pressures above 10 GPa. Furthermore, by coupling with the spontaneous strain, nonhydrostatic stresses can promote or suppress phase transitions (Decker et al. 1979; Resel et al. 2004), indicating that the previous studies cannot provide an adequate explanation about the structural characteristics of $SrSO_4$ at high pressures. In this study, neon is chosen as pressure-transmitting medium which provides a better hydrostatic environment in the sample chambers at pressures above 10 GPa. Even so, there is still no pressure-induced transition of $SrSO_4$ occurred within the pressure range in this study. These results clearly show that the crystal structure of $SrSO_4$ is stable at least at pressures lower than ~ 22.2 GPa. Furthermore, the previous studies have not observed any pressure-induced phase transition of $PbSO_4$ at pressures up to 35 GPa and 21.6 GPa, respectively (Lee et al. 2003; Li et al. 2018). Therefore, for better understanding the phase transition behavior of the barite-group minerals, future further investigations of $SrSO_4$ and $PbSO_4$ are highly needed at higher pressure.

Factors on the pressure-induced phase transition

From the above analysis, our results indicate that $BaSO_4$ undergoes a pressure-induced phase transition from *Pbnm* to $P2_12_12_1$ at ~ 20.3 GPa. However, the existing data show no pressure-induced phase transitions of $SrSO_4$ and $PbSO_4$ up to 22.2 GPa and 35 GPa, respectively. The bond length may be the most important factor on the phase transition pressure of barite-group minerals. In the crystal structure of barite-group minerals, each M^{2+} coordinates with 12 oxygen atoms, and each S atom is surrounded by four oxygen atoms to form SO_4 tetrahedron (Miyake et al. 1978). The radii of Sr^{2+}, Pb^{2+}, and Ba^{2+} are 1.44 Å, 1.49 Å, and 1. 61 Å, respectively (Shannon 1976). The average < M–O > distance increases with increasing ionic radius, and the corresponding average < M–O > distances for $SrSO_4$, $PbSO_4$, and $BaSO_4$ are 2.827 Å, 2.856 Å, and 2.953 Å (Antao 2012), respectively. Hence, the < Sr–O > distance is the shortest and the < Ba–O > distance is the longest, and the bonding force of < Sr–O > is the strongest, followed by those of < Pb–O > and < Ba–O>. In addition, the corresponding average < S–O > distances are 1.480 Å, 1.477 Å, and 1.471 Å (Miyake et al. 1978). Although the < S–O > distance decreases linearly with increasing cation ionic radius, the magnitude of the < S–O > distance variation is smaller than that of < M–O > distance variation, and the average of < S–O–S > angles of three barite-group minerals are nearly constant (109.5° for $SrSO_4$, 109.4° for $PbSO_4$, and 109.46° for $BaSO_4$). Therefore, < S–O > distances and < S–O–S > angles are less insensitive to pressure increase than that of < M–O > distances in the structure. When $SrSO_4$ is compressed, it needs to overcome more energy of < Sr–O > to convert into another more stable structure. Consequently, $SrSO_4$ may undergo a phase transition at a relatively higher pressure. The conjecture is consistent with the existing experimental results, where the phase transition pressure of $BaSO_4$ is ~ 20.3 GPa using neon as pressure-transmitting medium and the phase transition pressure of $PbSO_4$ is higher than ~ 35 GPa. However, the phase transition pressure of $SrSO_4$ may be even higher than that of $PbSO_4$. Therefore, among $BaSO_4$, $PbSO_4$, and $SrSO_4$, $SrSO_4$ has the highest phase transition pressure, and then, $PbSO_4$, and $BaSO_4$ has the lowest phase transition pressure.

Thermoelastic of barite-group minerals

Bulk modulus

The bulk moduli and their pressure derivatives of $BaSO_4$ and $SrSO_4$ in this study are 58 (2) GPa, 4.2 (2) and 64 (2) GPa, 4.8 (4), respectively. The bulk moduli of barite-group minerals under different pressure-transmitting media are summarized in Table 5 and the variation of bulk modulus with

Table 5 Elastic parameters of barite-group minerals

Samples	K_0 (GPa)	K_0'	References
Barite (He)	58.6 (2)	4.82 (4)	Santamaría-Pérez et al. (2011)
Barite (Silicone oil)	62 (1)	7.3 (4)	Santamaría-Pérez et al. (2011)
Barite (M:E = 4:1)	60.3 (9)	6.3 (2)	Santamaría-Pérez et al. (2011)
Barite (Theory)	62 (2)	4.5 (3)	Santamaría-Pérez et al. (2011)
Barite (No medium)	63 (2)	4 (fixed)	Lee et al. (2003)
Barite (He)	58.5 (20)	4.9 (3)	Crichton et al. (2011)
Barite (Neon)	58 (2)	4.2 (4)	This study
Barite (Neon)	60 (1)	4 (fixed)	This study
Celestite (Neon)	64 (2)	4.8 (4)	This study
Celestite (Neon)	68 (1)	4 (fixed)	This study
Celestite (M:E = 4:1)	87 (3)	4 (fixed)	Chen et al. (2010)
Celestite (M:E:W = 16:3:1)	62 (5)	11 (1)	Kuang et al. (2017)
Celestite (M:E:W = 16:3:1)	98 (2)	4 (fixed)	Kuang et al. (2017)
Anglesite (Neon)	59 (1)	5.3 (4)	Li et al. (2018)
Anglesite (Neon)	63.8 (7)	4 (fixed)	Li et al. (2018)

Numbers in parenthesis represent standard deviations

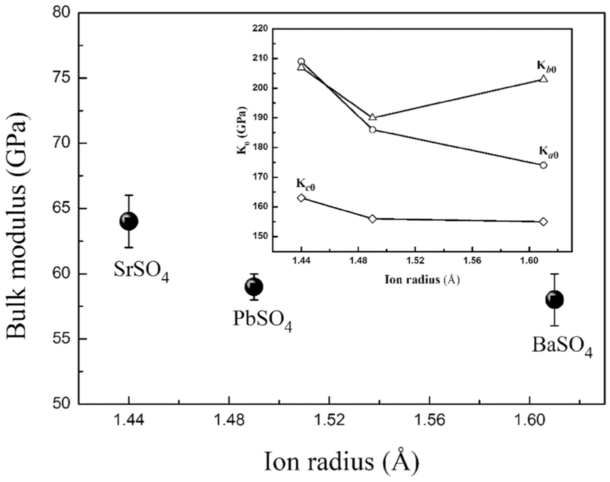

Fig. 13 Variations of the bulk modulus and linear modulus of barite-group minerals against ionic radius

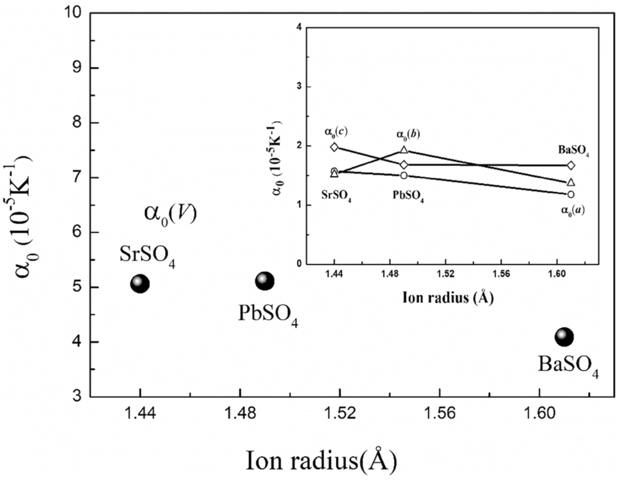

Fig. 14 Variation of the linear and volume thermal expansion coefficients of barite-group minerals with ion radius

effective size of ionic radius is shown in Fig. 13. Considering that neon can maintain a good hydrostatic environment, we chose the bulk moduli of $BaSO_4$ and $SrSO_4$ obtained in this study and the bulk modulus of $PbSO_4$ obtained by Li et al. (2018) for comparison. From Fig. 13, the bulk modulus of $SrSO_4$ is slightly higher than those of $BaSO_4$ and $PbSO_4$, where their bulk moduli are almost equal each other. In fact, the influencing factors on the compressibility of minerals are many and complicated. The effective size of M^{2+} cation, the bond length, the polarizability of the M element, the electronegativity, and the chemical valence are believed to be the factors on the compressibility of barite-group minerals (Zhang 1999; Liu et al. 2008; Fan et al. 2011, 2013; Li et al. 2018). The factors affecting the compressibility of barite-group minerals have been summarized by Li et al. (2018). In the light of the complexity of its impact, we believe that both geometrical and chemical factors actually influence the compressibility of barite-group minerals.

Volumetric thermal expansion

The volumetric thermal expansion coefficients at 300 K of $BaSO_4$ and $SrSO_4$ obtained in this study are 4.09×10^{-5} K^{-1} and 5.06×10^{-5} K^{-1}, respectively (Fig. 11). However, among the previous studies, only Fei (1995) recalculated the volumetric thermal expansion coefficient of $BaSO_4$ based on the data obtained from Sawada and Takéuchi (1990) and yielded $\alpha_V = 5.48 \times 10^{-5}$ K^{-1}, which is inconsistent with this study. Meanwhile, there are still no reports about the volumetric thermal expansion of $SrSO_4$. In addition, Li et al. (2018) also reported the volumetric thermal expansion coefficient of $PbSO_4$ at high temperatures. However, to ensure the reliability of comparison, we recalculate the volumetric thermal expansion coefficients of $PbSO_4$ using the data from Li et al. (2018) based on the expression proposed by Fei (1995) and obtain the $\alpha_V = 5.11 \times 10^{-5}\ K^{-1}$. Figure 14 shows the relationship between the volumetric thermal expansion coefficients and the effective size of ionic radius of barite-group minerals, which suggests that the volumetric thermal expansion coefficients seem to be decreasing within increasing ionic radius. The effective ionic radii of Sr^{2+}, Pb^{2+}, and Ba^{2+} are 1.44 Å, 1.49 Å, and 1.61 Å, respectively (Shannon 1976) and the corresponding average < M–O > distances for $SrSO_4$, $PbSO_4$, and $BaSO_4$ are 2.827 Å, 2.856 Å, and 2.953 Å (Antao 2012). Therefore, we infer that bond length may be a major factor affecting the volumetric thermal expansion of barite-group minerals.

Axial compressibility

The axial compressibility of $BaSO_4$ and $SrSO_4$ is also obtained in this study (Table 6). The variations of lattice parameters *a, b*, and *c* of $BaSO_4$ and $SrSO_4$ with pressure are shown in Fig. 10. These results clearly indicate that there is a different axial compression anisotropy between $BaSO_4$ and $SrSO_4$. The *b*-axis in both $BaSO_4$ and $SrSO_4$ is the most incompressible, and the axial compressibility of $BaSO_4$ along *a*- and *c*-axes is almost equivalent, but the axial compressibility of $SrSO_4$ along *c*-axis is higher than *a*-axis. Moreover, the minimal axial compressibility of all three barite-group minerals ($SrSO_4$, $BaSO_4$, and $PbSO_4$) is along the *b*-axis (Table 6). This phenomenon may be caused by the different bonding distances between M and SO_4 among the three crystallographic axes. The *b*-axis is the longest crystallographic axis in the barite-group minerals, but the distance between M and SO_4 is minimal, and then results in the maximum bonding force between M and SO_4. Therefore, when external force like pressure is applied to these minerals, the *b*-axis reflects the minimum axial compressibility.

Table 6 Axial compressibility moduli along *l*-axial (*l* = *a, b, c*) of barite-group minerals at room temperature

	l_0 (Å)	K_0 (GPa)	K_0'	References
Celestite				
a	6.864 (1)	209 (7)	13 (1)	This study
b	8.358 (1)	207 (7)	18 (2)	
c	5.348 (1)	163 (4)	13 (1)	
Barite				
a	7.1375 (2)	174 (5)	11 (1)	This study
b	8.8661 (4)	203 (5)	12 (1)	
c	5.4388 (3)	155 (4)	14 (1)	
Anglesite				
a	6.9493 (3)	186 (4)	13 (1)	Li et al. (2018)
b	8.4681 (4)	190 (5)	17 (1)	
c	5.3931 (2)	156 (4)	17 (1)	

Numbers in parenthesis represent standard deviations

In addition, Fig. 13 shows a comparison of the relationship between axial compressibility and ionic radius among the barite-group minerals. The axial moduli of *a*-axis and *c*-axis for the barite-group minerals decrease with increasing ionic radius; however, the variation tendency of *b*-axis with ionic radius is different, where the *b*-axis of $PbSO_4$ is the least compared with $SrSO_4$ and $BaSO_4$.

Axial thermal expansion

The axial thermal expansion coefficients of $BaSO_4$ and $SrSO_4$ at ambient conditions are also obtained in this study, $1.18 \times 10^{-5}\ K^{-1}$, $1.37 \times 10^{-5}\ K^{-1}$, $1.67 \times 10^{-5}\ K^{-1}$ and $1.57 \times 10^{-5}\ K^{-1}$, $1.52 \times 10^{-5}\ K^{-1}$, $1.98 \times 10^{-5}\ K^{-1}$ along *a*-, *b*-, and *c*-axes, respectively. Moreover, we also calculate the axial thermal expansion coefficients of $BaSO_4$ using the data of Sawada and Takéuchi (1990) as well and obtain $\alpha_a = 1.39 \times 10^{-5}\ K^{-1}$, $\alpha_b = 1.09 \times 10^{-5}\ K^{-1}$, and $\alpha_c = 2.49 \times 10^{-5}\ K^{-1}$ at ambient conditions, which are inconsistent with this study. Too large temperature interval and too few data points in the previous work may cause the difference. From Fig. 12, we conclude that the axial thermal expansion of $BaSO_4$ and $SrSO_4$ is slightly anisotropic. The axial thermal expansion along *c*-axis of $BaSO_4$ exhibits larger than those along *a*- and *b*-axes, but the *b*-axis of $SrSO_4$ has larger thermal expansion coefficient than those along *a*- and *b*-axes. Moreover, the compressibility and thermal expansion coefficient of $BaSO_4$ along *c*-axis are both largest, which is consistent with the result of Lee et al. (2003).

In addition, Table 7 summarizes the axial thermal expansivities of the barite-group minerals and Fig. 14 shows the variation of axial thermal expansion at 300 K with ionic radius. Obviously, the variation of the axial thermal expansions with ionic radius of these three barite-group minerals is different. The axial thermal expansion along *a*-axis of $SrSO_4$ and $PbSO_4$ is similar, but both of them are larger than that of $BaSO_4$. In addition, the axial thermal expansion along *b*-axis of $PbSO_4$ is also larger than that of $SrSO_4$ and $BaSO_4$. Moreover, the axial thermal expansion along *c*-axis of $BaSO_4$ and $PbSO_4$ is almost identical and smaller than that of $SrSO_4$. In a word, the axial thermal expansion of barite minerals is insensitive to ionic radius and there is no good correlation between the axial thermal expansion behavior and the axial compressibility of the barite-group minerals.

Table 7 Axial thermal expansivities along *l*-axial ($l = a, b, c$) of barite-group minerals at ambient pressure

	l_0	alph$_0$ ($\times 10^5$)	alph$_1$ ($\times 10^4$)	Alpha ($\times 10^5$)	References
Celestite					
a	6.858 (1)	1.14 (11)	1.45 (23)	1.57	This study
b	8.347 (1)	– 0.06 (11)	5.25 (24)	1.52	
c	5.343 (1)	1.49 (15)	1.63 (31)	1.98	
V	305.85 (4)	2.52 (24)	8.48 (51)	5.06	
Barite					
a	7.143 (1)	0.66 (6)	1.75 (12)	1.18	This study
b	8.866 (1)	0.92 (10)	1.50 (23)	1.37	
c	5.447 (1)	1.25 (11)	1.43 (24)	1.67	
V	345.10 (5)	2.52 (25)	5.25 (54)	4.09	
Anglesite					
a	6.948 (1)	1.31 (5)	0.63 (11)	1.50	Li et al. (2018)
b	8.468 (1)	1.15 (6)	2.60 (14)	1.92	
c	5.391 (1)	1.34 (8)	1.13 (19)	1.68	
V	317.20 (2)	3.82 (15)	4.31 (33)	5.11	

Numbers in parenthesis represent standard deviations

Conclusion

The phase transition and thermoelastic behavior of $BaSO_4$ and $SrSO_4$ have been investigated in the *P*–*T* range of 59.5 GPa, 700 K and 22.2 GPa, 700 K, respectively, using in situ synchrotron XRD combined with DACs. Our results confirm that $BaSO_4$ undergoes a pressure-induced phase transition at ~ 20.3 GPa from *Pbnm* to $P2_12_12_1$, but $SrSO_4$ does not in the *P*–*T* ranges. The bulk moduli and their pressure derivatives of $BaSO_4$ and $SrSO_4$ are derived from the *P*–*V* data. While their volumetric thermal expansion coefficients are derived from the *T*–*V* data. Our results show that $SrSO_4$ has anisotropic axial compressibility and axial thermal expansivity, but $BaSO_4$ has almost the same axial compressibility along *a*-axis and *c*-axis and relatively weak axial thermal expansivity. Furthermore, the influencing factors on the phase transition pressure of barite-group minerals are also discussed. The bond length of < M–O > may be the main factor which results in the maximum phase transition pressure of $SrSO_4$, compared with $PbSO_4$ and $BaSO_4$. Our results also show that geometrical and chemical factors influence the compressibility of barite-group minerals together and bond length may be the major factor affecting the volumetric thermal expansion of barite-group minerals. In addition, there is no good correlation between the axial thermal expansion behavior and the axial compressibility of the barite-group minerals.

Acknowledgements We are grateful to the beamline scientist of BL15U1 of SSRF and 4W2 of BSRF for the technical help. We also acknowledge HYS for the Neon gas-loading assistance. This project was supported by the National Natural Science Foundation of China (Grant nos. 41772043 and 41802043), the Joint Research Fund in Huge Scientific Equipment (U1632112) under cooperative agreement between NSFC and CAS, the Chinese Academy of Sciences "Light of West China" Program (Dawei Fan, 2017), Youth Innovation Promotion Association CAS (Dawei Fan, 2018434), and the CPSF-CAS Joint Foundation for Excellent Postdoctoral Fellows (Grant no. 2017LH014). The high-pressure XRD experiments were performed at the High-Pressure Experiment Station (4W2), Beijing Synchrotron Radiation Facility (BSRF), and the BL15U1 of the Shanghai Synchrotron Radiation Facility (SSRF).

References

Angel RJ (2000) Equations of state. Rev Miner Geochem 41:35–59. https://doi.org/10.2138/rmg.2000.41.2

Antao SM (2012) Structural trends for celestite ($SrSO_4$), anglesite ($PbSO_4$), and barite ($BaSO_4$): confirmation of expected variations within the SO_4 groups. Am Miner 97:661–665. https://doi.org/10.2138/am.2012.3905

Birch F (1947) Finite elastic strain of cubic crystals. Phys Rev 71:809–824. https://doi.org/10.1103/PhysRev.71.809

Borg IY, Smith DK (1975) A high pressure polymorph of $CaSO_4$. Contrib Miner Petrol 50:127–133. https://doi.org/10.1007/BF00373332

Canil D, Fellows SA (2017) Sulphide–sulphate stability and melting in subducted sediment and its role in arc mantle redox and chalcophile cycling in space and time. Earth Planet Sci Lett 470:73–86. https://doi.org/10.1016/j.epsl.2017.04.028

Chen YH, Yu SC, Huang E, Lee PL (2010) Raman spectroscopy and X-ray diffraction studies on celestite. Phys B Condens Matter 405:4386–4388. https://doi.org/10.1016/j.physb.2010.08.001

Crichton WA, Parise JB, Antao SM, Grzechnik A (2005) Evidence for monazite-, barite-, and $AgMnO_4$ (distorted barite)-type structures of $CaSO_4$ at high pressure and temperature. Am Miner 90:22–27. https://doi.org/10.2138/am.2005.1654

Crichton WA, Merlini M, Hanfland M, Muller H (2011) The crystal structure of barite, $BaSO_4$, at high pressure. Am Miner 96:364–367. https://doi.org/10.2138/am.2011.3656

Decker DL, Petersen S, Debray D, Lambert M (1979) Pressure-induced ferroelastic phase transition in $Pb_3(PO_4)_2$: a neutron-diffraction study. Phys Rev B 19:3552–3555. https://doi.org/10.1103/PhysRevB.19.3552

Evans KA (2012) The redox budget of subduction zones. Earth Sci Rev 113:11–32. https://doi.org/10.1016/j.earscirev.2012.03.003

Fan D, Zhou W, Wei S et al (2010) A simple external resistance heating diamond anvil cell and its application for synchrotron radiation X-ray diffraction. Rev Sci Instrum 81:053903. https://doi.org/10.1063/1.3430069

Fan D, Wei S, Liu J et al (2011) High pressure X-Ray diffraction study of a grossular—andradite solid solution and the bulk modulus variation along this solid solution. Chin Phys Lett 28:076101. https://doi.org/10.1088/0256-307X/28/7/076101

Fan D, Ma M, Wei S et al (2013) In-situ synchrotron powder X-ray diffraction study of vanadinite at room temperature and high pressure. High Temp High Press 42:441–449

Fan D, Xu J, Liu J et al (2014) Thermal equation of state of natural stibnite up to 25.7. High Temp High Press 43:351–359

Fan D, Xu J, Kuang Y et al (2015) Compressibility and equation of state of beryl ($Be_3Al_2Si_6O_{18}$) by using a diamond anvil cell and in situ synchrotron X-ray diffraction. Phys Chem Miner 42:529–539. https://doi.org/10.1007/s00269-015-0741-1

Fei Y (1995) Thermal expansion. In: Ahrens TJ (ed) Mineral physics & crystallography: a handbook of physical constants. American Geophysical Union, Washington, DC, pp 29–44

Fei Y, Ricolleau A, Frank M et al (2007) Toward an internally consistent pressure scale. Proc Natl Acad Sci 104:9182–9186. https://doi.org/10.1073/pnas.0609013104

Fujii T, Ohfuji H, Inoue T (2016) Phase relation of $CaSO_4$ at high pressure and temperature up to 90 GPa and 2300 K. Phys Chem Miner 43:353–361. https://doi.org/10.1007/s00269-016-0799-4

Garske D, Peacor DR (1965) Refinement of the structure of celestite $SrSO_4$*. Zeitschrift für Krist 121:204–210. https://doi.org/10.1524/zkri.1965.121.2-4.204

Gonzalez-Platas J, Alvaro M, Nestola F, Angel R (2016) EosFit7-GUI: a new graphical user interface for equation of state calculations, analyses and teaching. J Appl Crystallogr 49:1377–1382. https://doi.org/10.1107/S1600576716008050

Gracia L, Beltrán A, Errandonea D, Andrés J (2012) $CaSO_4$ and its pressure-induced phase transitions. A density functional theory study. Inorg Chem 51:1751–1759. https://doi.org/10.1021/ic202056b

Hammersley AP, Svensson SO, Hanfland M et al (1996) Two-dimensional detector software: from real detector to idealised image or two-theta scan. High Press Res 14:235–248. https://doi.org/10.1080/08957959608201408

Hemley RJ, Zha CS, Jephcoat AP et al (1989) X-ray diffraction and equation of state of solid neon to 110 GPa. Phys Rev B 39:11820–11827. https://doi.org/10.1103/PhysRevB.39.11820

Jégo S, Dasgupta R (2013) Fluid-present melting of sulfide-bearing ocean-crust: experimental constraints on the transport of sulfur from subducting slab to mantle wedge. Geochim Cosmochim Acta 110:106–134. https://doi.org/10.1016/j.gca.2013.02.011

Jégo S, Dasgupta R (2014) The fate of sulfur during fluid-present melting of subducting basaltic crust at variable oxygen fugacity. J Petrol 55:1019–1050. https://doi.org/10.1093/petrology/egu016

Kelley KA, Cottrell E (2009) Water and the oxidation state of subduction zone magmas. Science 325:605–607. https://doi.org/10.1126/science.1174156

Kuang Y, Kuang J, Zhao D et al (2017) The high-pressure elastic properties of celestine and the high pressure behavior of barite-type sulphates. High Temp High Press 46:481–495

Larson AC, Von Dreele RB (2004) General structure analysis system (GSAS). Los Alamos Natl Lab LAUR 86–748:1–179

Le Bail A, Duroy H, Fourquet JL (1988) Ab-initio structure determination of $LiSbWO_6$ by X-ray powder diffraction. Mater Res Bull 23:447–452. https://doi.org/10.1016/0025-5408(88)90019-0

Lee PL, Huang E, Yu SC (2003) High-pressure Raman and X-ray studies of barite, $BaSO_4$. High Press Res 23:439–450. https://doi.org/10.1080/0895795031000115439

Lee PL, Huang E, Yu SC, Chen YH (2013) High-pressure raman study on anglesite. World J Condens Matter Phys 03:28–32. https://doi.org/10.4236/wjcmp.2013.31005

Li B, Xu J, Chen W et al (2018) Compressibility and expansivity of anglesite ($PbSO_4$) using in situ synchrotron X-ray diffraction at high-pressure and high-temperature conditions. Phys Chem Miner 45:883–893. https://doi.org/10.1007/s00269-018-0970-1

Liu X, Shieh SR, Fleet ME, Akhmetov A (2008) High-pressure study on lead fluorapatite. Am Miner 93:1581–1584. https://doi.org/10.2138/am.2008.2816

Miyake M, Minato I, Morikawa H, Iwai S (1978) Crystal structures and sulphate force constants of barite, celestite, and anglesite. Am Miner 63:506–510

Mungall JE (2002) Roasting the mantle: Slab melting and the genesis of major Au and Au-rich Cu deposits. Geology 30:915. https://doi.org/10.1130/0091-7613(2002)030%3C0915:RTMSMA%3E2.0.CO;2

Resel R, Oehzelt M, Shimizu K et al (2004) On the phase-transition in anthracene induced by high pressure. Solid State Commun 129:103–106. https://doi.org/10.1016/j.ssc.2003.09.019

Richards JP (2011) Magmatic to hydrothermal metal fluxes in convergent and collided margins. Ore Geol Rev 40:1–26. https://doi.org/10.1016/j.oregeorev.2011.05.006

Santamaría-Pérez D, Gracia L, Garbarino G et al (2011) High-pressure study of the behavior of mineral barite by X-ray diffraction. Phys Rev B 84:054102. https://doi.org/10.1103/PhysRevB.84.054102

Sawada H, Takéuchi Y (1990) The crystal structure of barite, β-$BaSO_4$, at high temperatures. Zeitschrift für Krist Cryst Mater 191:161–171. https://doi.org/10.1524/zkri.1990.191.3-4.161

Shannon RD (1976) Revised effective ionic radii and systematic studies of interatomic distances in halides and chalcogenides. Acta Crystallogr Sect A 32:751–767. https://doi.org/10.1107/S0567739476001551

Tomkins AG, Evans KA (2015) Separate zones of sulfate and sulfide release from subducted mafic oceanic crust. Earth Planet Sci Lett 428:73–83. https://doi.org/10.1016/j.epsl.2015.07.028

Wang J, Bass JD, Kastura T (2014) Elastic properties of iron-bearing wadsleyite to 17.7 GPa: Implications for mantle mineral models. Phys Earth Planet Inter 228:92–96. https://doi.org/10.1016/j.pepi.2014.01.015

Xia X, Weidner DJ, Zhao H (1998) Equation of state of brucite; single-crystal Brillouin spectroscopy study and polycrystalline pressure-volume-temperature measurement. Am Miner 83:68–74. https://doi.org/10.2138/am-1998-1-207

Zhang J (1999) Room-temperature compressibilities of MnO and CdO: further examination of the role of cation type in bulk modulus systematics. Phys Chem Miner 26:644–648. https://doi.org/10.1007/s002690050229

Zhang J (2009) High-pressure Raman and X-ray studies of barite, $BaSO_4$. High Press Res 23:439–450. https://doi.org/10.1080/0895795031000115439

Publisher's Note Springer Nature remains neutral with regard to jurisdictional claims in published maps and institutional affiliations.